EULER INVERSE THROUGHFLOW MODEL BASED ON AN IMPLICIT UPWIND TIME MARCHING TECHNIQUE

S. Rosa Taddei*, F. Larocca*, F. Bertini**, E. Spano**
*Politecnico di Torino (I) - Dipartimento di Ingegneria aeronautica e spaziale, **Avio Group Italy

Keywords: *Euler, implicit, inverse, throughflow, upwind*

Abstract

The model prescribes the meridional loading distribution over the blade regions. It predicts the axisymmetric flowfield and related hub-to-tip streamsurface geometry. The implicit approach is meant to reach the steady solution more quickly, but most of all to carry the enforcement of the mass flowrate at the outlet section. This allows the numerical procedure to design high camber turbine blades. The capabilities of the method in dealing with single strong deflection cascades and a complete turbine stage are proved.

1 Introduction

Despite the increasing computational resources, full three-dimensional flow simulations are still far from being routinely used for the analysis of complete multistage turbomachinery. Throughflow models remain essential tools in the aerodynamic design process, especially from an industrial point of view. Over the past 15 years, several attempts have been made in order to use CFD-based methodologies for throughflow computations. The latest generation throughflow models replace the classical streamline curvature and streamfunction methods with time marching solutions of either Euler [1], [2], [3] or Navier-Stokes [4] axisymmetric equations (eqs.). In these models, the blades come down to hub-to-tip streamsurfaces. Their turning effect on the flow is obtained through a blade force field that acts normally to the surfaces.

The purpose of the present work is to widen to turbine design the inverse model addressed by reference (ref.) [5] for axial compressor design. The model requires the tangential component of the blade force field, that is, the blade loading distribution, as design data. It predicts the axisymmetric flowfield and draws the corresponding hub-to-tip streamsurface geometry from the surface-flow slip equation. The loading distribution can be set up through an inverse optimization process, with various cost functions, but constrained by single stage power.

The extension of the model to high blade loadings and the typical flow deflections of current aeronautical turbines is not straightforward. Ref. [6] proves that when the Euler eqs. are solved with conventional boundary conditions, such as total quantities and flow angle at the inlet section and static pressure at the outlet section, the time marching procedure can only lead to low deflection cascades. The same ref. proposes one method to overcome the matter, by introducing a discontinuity surface at the outlet section. On the other hand, ref. [7] shows that a way to numerically obtain any theoretical inverse solution of the ideal (i.e., zero thickness and pitch) cascade problem, at least in principle, is to replace the static pressure with the mass flowrate at the outlet section. Unfortunately, the reflectiveness of this boundary condition increases very much with the Mach number [8] and allows the upwind explicit schemes of refs. [6], [9] and [5] to converge only for moderate camber and loading turbine cascades. In order to partly overcome the problem, a non-reflective formulation of the boundary condition can be adopted, which re-

quires a calibration process [10]. However, the limits of this approach will be shown by the paper.

Here, keeping the mass flowrate as outlet condition, we prefer to trust the inherent numerical stability properties of an implicit upwind time marching procedure. Details on the implicit discretization of the Euler eqs. and surface-flow slip eq. are given in sections (secs.) 3 and 4, respectively. Sec. 2 recalls the formulation of our throughflow model. In secs. 5 and 6, the implicit scheme is applied to both the one-dimensional and complete axisymmetric formulations of the inverse problem, through the design of two infinite span ideal cascades and a turbine stage.

2 The inverse throughflow model

Our Euler throughflow model shares the same basic idea as classical throughflow calculations, where the blades come down to hub-to-tip S2 streamsurfaces [11]. Together with the blade force source term, the axisymmetric Euler eqs. contain further terms modeling the blade-to-blade blockage and profile loss effects.

The model is described by a set of eqs. written in cylindrical coordinates for an inertial frame. In the rest of the paper, each quantity will be normalized to conventional reference values.

Surface-flow slip equation During the transient, this eq. governs the waving motion of each streamsurface around its leading edge:

$$\frac{\partial \vartheta}{\partial t} + u\frac{\partial \vartheta}{\partial x} + v\frac{\partial \vartheta}{\partial r} = \frac{w}{r} - \omega \qquad (1)$$

The leading edge shape in the tangential plane, that is, the blade lean, has to be prescribed as a boundary condition.

Euler equations These are expressed in the conservative form

$$\frac{\partial\{W\}}{\partial t} + \frac{\partial\{F\}}{\partial x} + \frac{\partial\{G\}}{\partial r} = \{Q_0\} + \{Q_b\} + \{Q_h\} + \{Q_v\} \qquad (2)$$

where the conservative variable vector, the convective flux vectors and the inertial source term keep the usual expressions:

$$\{W\} = \rho\begin{pmatrix}1 & u & v & w & E^0\end{pmatrix}^T$$

$$\{F\} = \rho u\begin{pmatrix}1 & \dfrac{p}{\rho u}+u & v & w & H^0\end{pmatrix}^T$$

$$\{G\} = \rho v\begin{pmatrix}1 & u & \dfrac{p}{\rho v}+v & w & H^0\end{pmatrix}^T$$

$$\{Q_0\} = -\frac{\rho v}{r}\begin{pmatrix}1 & u & v-\dfrac{w^2}{v} & 2w & H^0\end{pmatrix}^T$$

The present flow model is actually marked by the other three source terms, that include the blade force field, the blockage model and the viscous force field:

$$\{Q_b\} = \begin{pmatrix}0 & f_{bx} & f_{br} & f_{b\vartheta} & \vec{f}_b\cdot\vec{V}\end{pmatrix}^T$$

$$\{Q_h\} = -\frac{\rho u}{h}\frac{\partial h}{\partial x}\begin{pmatrix}1 & u & v & w & H^0\end{pmatrix}^T$$

$$\{Q_v\} = \begin{pmatrix}0 & f_{vx} & f_{vr} & f_{v\vartheta} & f_{v\vartheta}\,\omega r\end{pmatrix}^T$$

where the free passage per unit tangential length, $h = 1 - \frac{n\delta_\vartheta(x,r)}{2\pi}$, is prescribed as design data. The viscous force field $\vec{f}_v$ is opposite the direction of the relative flow motion. Through the distributed loss model, it is meant to enforce the profile loss drop of relative total pressure along the meridional streamlines [12].

Blade force equation This enforces the orthogonality between the blade force field and the streamsurface ϑ:

$$\vec{f}_b = f_{b\vartheta}\left(-r\frac{\partial \vartheta}{\partial x}\vec{i} - r\frac{\partial \vartheta}{\partial r}\vec{j} + \vec{k}\right) \qquad (3)$$

Since the vector eq. (3) gives rise to only two scalar eqs., one among the nine quantities $\vartheta, \rho, p, \vec{V}, \vec{f}_b$ must be given in order to close the axisymmetric problem. In the direct/analysis formulations this is obviously the streamsurface $\vartheta(x,r)$, which on the contrary becomes an outcome for any inverse/design formulation. Inverse throughflow models allow the designer to select a

design requirement to be fulfilled by the stream-surface geometry. Our model prescribes the tangential blade force distribution $f_{b\vartheta}(x,r)$. By definition of a blade force, this involves the meridional shaft power distribution over the rotor regions and, more generally, the meridional shaft torque distribution over any blade region.

3 The implicit upwind scheme

Our finite volume implicit scheme is based on a Newton linearization of the numerical flux vectors [13]. When the linearization is applied to the conservation laws (2) for the ij-th cell of the phisyical plane xr, it leads us to write

$$\begin{aligned}
&\left[C_{i,j-1}\right]\{\Delta W_{i,j-1}\}+\left[C_{i-1,j}\right]\{\Delta W_{i-1,j}\}\\
&\qquad+\left[C_{ij}\right]\{\Delta W_{i,j}\}\\
&+\left[C_{i+1,j}\right]\{\Delta W_{i+1,j}\}+\left[C_{i,j+1}\right]\{\Delta W_{i,j+1}\}=\\
&\quad-\Delta\ell_{i+\frac{1}{2},j}\{\mathcal{F}_{i+\frac{1}{2},j}\}+\Delta\ell_{i-\frac{1}{2},j}\{\mathcal{F}_{i-\frac{1}{2},j}\}\\
&\quad-\Delta\ell_{i,j+\frac{1}{2}}\{\mathcal{F}_{i,j+\frac{1}{2}}\}+\Delta\ell_{i,j-\frac{1}{2}}\{\mathcal{F}_{i,j-\frac{1}{2}}\}\\
&+\Delta\sigma_{ij}\left(\{Q_{0,ij}\}+\{Q_{b,ij}\}+\{Q_{h,ij}\}+\{Q_{v,ij}\}\right)
\end{aligned}\tag{4}$$

where

$$\left[C_{i,j-1}\right]=-\Delta\ell_{i,j-\frac{1}{2}}\left[\frac{\partial\mathcal{F}_{i,j-\frac{1}{2}}}{\partial W_{i,j-1}}\right]$$

$$\left[C_{i,j-1}\right]=-\Delta\ell_{i-\frac{1}{2},j}\left[\frac{\partial\mathcal{F}_{i-\frac{1}{2},j}}{\partial W_{i-1,j}}\right]$$

$$\begin{aligned}
\left[C_{ij}\right]&=\frac{\Delta\sigma_{ij}}{\Delta t_{ij}}[I]\\
&-\Delta\ell_{i,j-\frac{1}{2}}\left[\frac{\partial\mathcal{F}_{i,j-\frac{1}{2}}}{\partial W_{ij}}\right]-\Delta\ell_{i-\frac{1}{2},j}\left[\frac{\partial\mathcal{F}_{i-\frac{1}{2},j}}{\partial W_{ij}}\right]\\
&+\Delta\ell_{i+\frac{1}{2},j}\left[\frac{\partial\mathcal{F}_{i+\frac{1}{2},j}}{\partial W_{ij}}\right]+\Delta\ell_{i,j+\frac{1}{2}}\left[\frac{\partial\mathcal{F}_{i,j+\frac{1}{2}}}{\partial W_{ij}}\right]
\end{aligned}$$

$$\left[C_{i+1,j}\right]=\Delta\ell_{i+\frac{1}{2},j}\left[\frac{\partial\mathcal{F}_{i+\frac{1}{2},j}}{\partial W_{i+1,j}}\right]$$

$$\left[C_{i,j+1}\right]=\Delta\ell_{i,j+\frac{1}{2}}\left[\frac{\partial\mathcal{F}_{i,j+\frac{1}{2}}}{\partial W_{i,j+1}}\right]$$

It should be noted that a variable time step is adopted over the domain, in order to speed up the convergence of the scheme to the steady solution [14].

3.1 First-order space accurate scheme

We start from the right hand side of eq. (4). In order to compute, for instance, the numerical flux $\{\mathcal{F}_{i+\frac{1}{2},j}\}$, a one-dimensional Riemann problem (or shock tube problem) is approximately solved in the direction normal to the interface $i+\frac{1}{2},j$. Let φ be the angle between this direction and the x axis, so that

$$\cos\phi=\frac{r_{ij}-r_{i,j-1}}{\Delta\ell_{i+\frac{1}{2},j}}\qquad\sin\phi=\frac{x_{i,j-1}-x_{ij}}{\Delta\ell_{i+\frac{1}{2},j}}$$

If $\{U\}$ denotes the primitive variable vector $(a\quad u\quad v\quad w\quad S)^T$, for first-order space accuracy, i.e. $\{U\}=const$ in each cell, the initial states of the Riemann problem will be

$$\{U'_{ij}\}=\left[\mathcal{R}_{i+\frac{1}{2},j}\right]\{U_{ij}\}$$

$$\{U'_{i+1,j}\}=\left[\mathcal{R}_{i+\frac{1}{2},j}\right]\{U_{i+1,j}\}$$

where

$$\left[\mathcal{R}_{i+\frac{1}{2},j}\right]=\left[\frac{\partial U'_{ij}}{\partial U_{ij}}\right]=\left[\frac{\partial U'_{i+1,j}}{\partial U_{i+1,j}}\right]=$$

$$\begin{pmatrix}
1 & 0 & 0 & 0 & 0\\
0 & \cos\varphi & \sin\varphi & & \\
0 & -\sin\varphi & \cos\varphi & 0 & 0\\
0 & 0 & 0 & 1 & 0\\
0 & 0 & 0 & 0 & 1
\end{pmatrix}$$

Suppose for the moment that the Riemann problem has already been solved. Consistently with the Osher's flux difference splitting method [15], the numerical flux on the interface $i+\frac{1}{2},j$ involves the fluxes in each of the six regions defined by the solution:

$$\begin{aligned}
&\{\mathcal{F}_{i+\frac{1}{2},j}\}=\frac{1}{2}\left(\{\mathcal{F}_{ij}\}+\{\mathcal{F}_{i+1,j}\}\right)\\
&-\frac{1}{2}\int_i^{i+1}\left[V^{-1}\right]\left(\left[\Lambda^+\right]-\left[\Lambda^-\right]\right)[V]\,\mathrm{d}\{W\}\simeq\\
&\qquad\frac{1}{2}\left(\{\mathcal{F}_{ij}\}+\{\mathcal{F}_{i+1,j}\}\right)\\
&-\frac{1}{2}\left(\sum_{k=1}^{5}\operatorname{sgn}\lambda_k\left(\{\mathcal{F}_{i+\frac{k}{5},j}\}-\{\mathcal{F}_{i+\frac{k-1}{5},j}\}\right)\right)
\end{aligned}\tag{5}$$

where $[\Lambda^-]$, $[\Lambda^+]$ and $[V]$ are the negative eigenvalues, positive eigenvalues and right eigenvectors matrices of the jacobian matrix (j.m.) $[\partial\mathcal{F}/\partial W]$. Denoted by $\{U'\}$ the primitive variable vector in a generic region, to compute the corresponding flux vector the rotation $[\mathcal{R}_{i+\frac{1}{2},j}]^{-1}$ has to be applied, which gives

$$\{\mathcal{F}\} = \begin{pmatrix} \rho' u' \\ p'\cos\varphi + \rho' u'(\cos\varphi u' - \sin\varphi v') \\ p'\sin\varphi + \rho' u'(\sin\varphi u' + \cos\varphi v') \\ \rho' u' w' \\ \rho' u' \left(\frac{a'}{\gamma-1} + \frac{u'^2+v'^2+w'^2}{2}\right) \end{pmatrix} \tag{6}$$

Extending these concepts to the implicit part of the scheme (4) is straightforward. The j.m. $[\partial\mathcal{F}_{i,j+\frac{1}{2}}/\partial W_{ij}]$, for instance, can be obtained from expression (5) through derivation. To evaluate the j.m. in each region, we break it up into four j.ms. involving elementary transformations:

$$\left[\frac{\partial\mathcal{F}_{i+\frac{k}{5},j}}{\partial W_{ij}}\right] = \left[\frac{\partial\mathcal{F}_{i+\frac{k}{5},j}}{\partial U'_{i+\frac{k}{5},j}}\right]\left[\frac{\partial U'_{i+\frac{k}{5},j}}{\partial U'_{ij}}\right] \cdot \left[\mathcal{R}_{i+\frac{1}{2},j}\right]\left[\frac{\partial U_{ij}}{\partial W_{ij}}\right] \tag{7}$$

The first j.m. is obtained from derivation of the expression (6) whereas the last simply represents a variable change in the ij-th cell. The second j.m. accounts for the Riemann problem solution, expressed through the primitive variables. Its structure relates to the approximated method which is chosen to solve the Riemann problem at the interface $i+\frac{1}{2}, j$.

The other flux vectors that appear in the scheme (4) and their j.ms. are computed in a similar way.

3.2 Approximate solution of the Riemann problem

Several methods have been proposed to obtain an accurate and efficient approximation of the Riemann problem solution at the interface between two contiguous cells. We adopted the approach of ref. [16]. Here, the indexes $k=2$ and $k=3$ denote the two regions divided by a contact surface (u' wave family) whereas $k=1$ and $k=4$ denote the two sonic regions associated with the $u'-a'$ and $u'+a'$ acoustic wave families, respectively. Therefore, for the coefficients of the splitting (5) we have

$$\lambda_1 = u'_i - a'_i \qquad \lambda_2 = u'_{i+\frac{1}{5}} - a'_{i+\frac{1}{5}}$$
$$\lambda_3 = u'_{i+\frac{2}{5}} = u'_{i+\frac{3}{5}}$$
$$\lambda_4 = u'_{i+\frac{4}{5}} + a'_{i+\frac{4}{5}} \qquad \lambda_5 = u'_{i+1} + a'_{i+1}$$

The parallel and tangential speed components v' and w' are supposed to keep along the contact surface, together with entropy. It is easy to show, in fact, that $u' = \cos\varphi u + \sin\varphi v$ is a 3-multiplicity eigenvalue of the matrix $\cos\varphi[\partial F/\partial W] + \sin\varphi[\partial G/\partial W]$ [17], associated with the Riemann variables $S' = S$ (as in the one-dimensional Euler eqs.), $w' = w$ and $v' = -\sin\varphi u + \cos\varphi v$. We point out that, because of the source terms in eqs. (2), these variables cannot be actually considered as Riemann invariants for the u' waves.

3.3 Boundary conditions

Our scheme allows a simple enforcement of physical boundary conditions consistently with its upwind spirit. At the boundary interfaces, a partial Riemann problem has to be solved, where some regions disappear and one condition carried by each incoming wave replaces information from the missing cell. For subsonic axisymmetric flow, only one condition is needed along the outlet section whereas four conditions are needed along the inlet section. As we previously explained, in our model the former is the unit mass flowrate ρu (prescribed in the general reflective formulation), whereas the latter are two total quantities and the ramp and blade-to-blade flow angles. For the endwall interfaces we prescribe the slip condition $v' = 0$.

The j.ms. $[\partial U'/\partial U']$ in the product (7) are modified to account for the partial Riemann problem solution at the boundary interfaces. Since the derivation process requires this solution to be expressed in closed form, we adopt space linearized boundary conditions whenever it is necessary.

3.4 Second-order space accurate scheme

To make the scheme second-order space accurate is straightforward. A linear variation of the primitive variables in both the grid directions is assumed over each cell, then a high order solution of the Riemann problem is evaluated. At the interface $i+\frac{1}{2}, j$, the initial states of the problem will become $\{U'_{ij}\}+0.5\{\Delta^i U'_{ij}\}$ and $\{U'_{i+1,j}\}-0.5\{\Delta^i U'_{i+1,j}\}$, where $\{\Delta^i U_{ij}\}$ is defined through a minmod limiter:

$$\{\Delta^i U_{ij}\} = \text{minmod}\left(\{U_{ij}\}-\{U_{i-1,j}\},\ \{U_{i+1,j}\}-\{U_{ij}\}\right)$$

For the boundary cells, we replace missing information with the primitive variable values that were predicted by the latest solution of the Riemann problem on the boundary interface.

Since we are not interested in the transient solution, we accepted the approximation $0.5|[\partial\Delta^i U_{ij}/\partial U_{ij}]| << [I]$, that is, we left the product (7) formally unchanged. An investigation should be made, in order to verify that such simplification does not affect the TVD and ENO properties owned by the predictor-corrector explicit scheme of ref. [5]. These properties are proved in ref. [18].

4 Update of the blade geometry

Once the new flowfield has been predicted by the finite volume scheme, the blade geometry is updated through integration of eq. (1). Since this does not have a corresponding conservation law, it requires a finite difference discretization in the computational plane $\xi\eta$, with the grid nodes placed in the cell centers. Therefore we have

$$\frac{\partial\vartheta}{\partial t}+\tilde{u}\frac{\partial\vartheta}{\partial\xi}+\tilde{v}\frac{\partial\vartheta}{\partial\eta}=\frac{w}{r}-\omega \qquad (8)$$

where

$$\tilde{u}=u\frac{\partial\xi}{\partial x}+v\frac{\partial\xi}{\partial r} \qquad \tilde{v}=u\frac{\partial\eta}{\partial x}+v\frac{\partial\eta}{\partial r}$$

In order to carry the high CFL values allowed by the Euler solver, eq. (8) is integrated in time through an implicit upwind finite difference scheme. No boundary condition is required at each blade exit whereas blade lean is prescribed along the leading edges. For the cells contiguous to the endwalls, the normal derivative $\partial\vartheta/\partial\eta$ is computed from the interior of the domain. We notice that a discretization of eq. (8) in the cell apexes, instead of their centers, would allow us to remove such derivative from the endwalls nodes. In these, in fact, it would be possible to enforce the characteristic condition $\tilde{v}=0$, which is equivalent to the slip condition $v/u=\mathrm{d}r/\mathrm{d}x$. However, we believe that, for both the explicit and implicit time marching procedures, the loss of upwind spirit for the endwall cells can cause further numerical instability at high flow deflections. One method to overcome the problem lies in adopting a finite difference discretization also for Euler eqs. (2), with the cell apexes as grid nodes. The finite difference formulation of our implicit upwind scheme is proposed in ref. [13].

After the new solution of eq. (8) has been computed, the same upwind discretization of the derivatives $\partial\vartheta/\partial\xi$ and $\partial\vartheta/\partial\eta$ is used to update the axial and radial components of the blade force field from the vector eq. (3). Our procedure shares this passage with the explicit procedure of ref. [5].

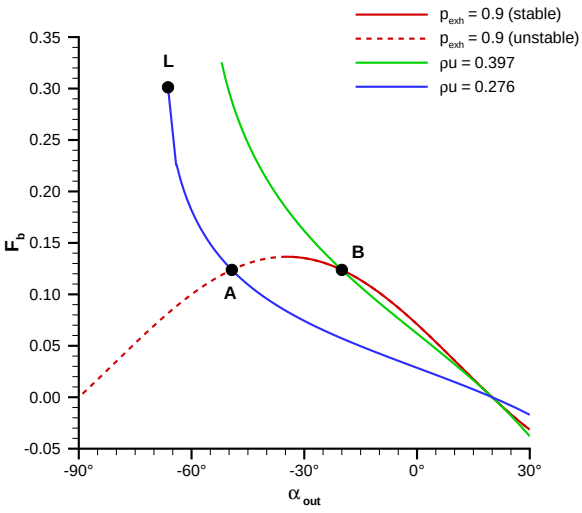

Fig. 1 Theoretical solution for the cascades B, A and L

5 The ideal cascade inverse problem

Besides the complete axisymmetric formulation of the inverse problem, a simpler one-dimensional formulation exists, which is meant to design an infinite span, zero thickness and pitch cascade. Now, eqs. (1)-(3) are written in cartesian coordinates but any derivative along the spanwise coordinate y must be suppressed. For a stator cascade we have

$$\begin{aligned} \frac{\partial z}{\partial t} + u\frac{\partial z}{\partial x} &= w \\ \frac{\partial \{W\}}{\partial t} + \frac{\partial \{F\}}{\partial x} &= \{Q_b\} + \{Q_h\} + \{Q_v\} \\ \vec{f}_b &= f_{bz}\left(-\frac{\partial z}{\partial x}\vec{i} + \vec{k}\right) \end{aligned} \qquad (9)$$

where

$$\begin{aligned} \{W\} &= \rho\begin{pmatrix} 1 & u & w & E^0 \end{pmatrix}^T \\ \{F\} &= \rho u\begin{pmatrix} 1 & \dfrac{p}{\rho u} + u & w & H^0 \end{pmatrix}^T \\ \{Q_b\} &= \begin{pmatrix} 0 & f_{bx} & f_{bz} & \vec{f}_b \cdot \vec{V} \end{pmatrix}^T \\ \{Q_h\} &= -\frac{\rho u}{h}\frac{\mathrm{d}h}{\mathrm{d}x}\begin{pmatrix} 1 & u & w & H^0 \end{pmatrix}^T \\ \{Q_v\} &= \begin{pmatrix} 0 & f_{vx} & f_{vz} & 0 \end{pmatrix}^T \end{aligned}$$

The free passage per unit tangential length h is defined as $1 - \frac{\sigma_x \delta_z(x)}{c_x}$.

When $\vec{f}_v = 0$, the theoretical steady solution of eqs. (9) can be computed, although not in closed form. However, ref. [6] proves that the time marching procedure is able to re-obtain only the solutions that obey the stability condition

$$\frac{\partial F_b}{\partial \alpha_{out}} < 0 \qquad (10)$$

where $F_b = -\int_{x_{le}}^{x_{te}} f_{bz}(x)h(x)\,\mathrm{d}x$ is the blade loading. Figure (fig.) 1 shows three F_b-α_{out} diagrams computed for $\alpha_{inl} = 20^o$, $T^0_{inl} = 1$ and $p^0_{inl} = 1$. In view of the condition (10), the low deflection cascade B can be numerically obtained by prescribing either $p = 0.9$ or $\rho u = 0.397$ at the outlet section; the high deflection cascade A and, even more so, the limit loading (i.e., sonic outlet) cascade L can be only re-obtained by prescribing $\rho u = 0.276$. As proved in ref. [6], the explicit procedure, with the static pressure as outlet condition, efficiently reaches the cascade B.

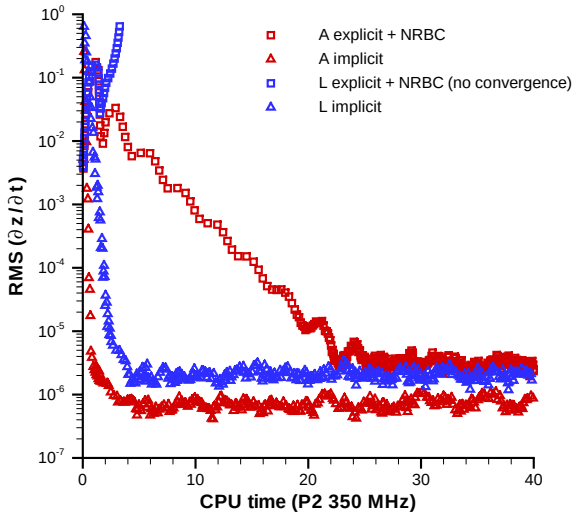

Fig. 2 Convergence history for the cascades A and L

Whenever we replace the static pressure with the mass flowrate, some trick has to be introduced into the explicit procedure in order to ensure its numerical stability. We compared our implicit scheme to the explicit scheme of ref. [5], but coupled to a partially non-reflective formulation of the outlet condition, in the spirit of ref. [10]. The explicit scheme works with CFL=2 [18], whereas the implicit scheme works with CFL=300. Fig. 2 shows the convergence histories to the cascades A and L of fig. 1. The explicit scheme does not converge to the limit loading solution, since the non-reflective outlet condition is only efficient for low Mach numbers ($M_{out,A} = M_{out,B} \simeq 0.4$). However, even when both the schemes are stable, the implicit procedure allows us to gain one order in convergence time and level. We notice that the implicit discretization of the first and second eqs. (9) gives rise to tridiagonal matrix systems, which can be efficiently solved by the Thomas algorithm. For two-dimensional flow, these matrices become pentadiagonal, and in principle could be treated by approximate factorization methods, that involve 10-15 maximum CFL values. Unfortunately, near the limit load-

ings the implicit scheme has resulted to be unstable *under* CFL$\simeq$100. Most likely, this lower bound relates to the need of jumping over the strong transients that arise when we realize very high flow deflections.

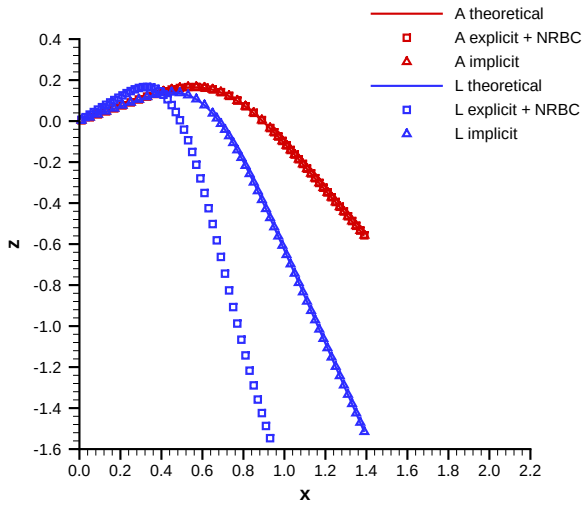

Fig. 3 Streamline geometry the for cascades A and L

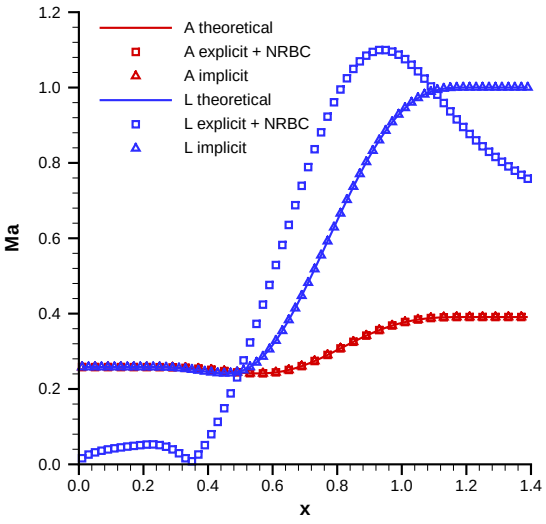

Fig. 4 Mach number for the cascades A and L

Fig. 3 and 4 display the streamline geometries and Mach number profiles. The explicit L solution has no physical meaning. In both tests the blade loading distribution $-f_{bz}(x)$, with $x_{le} = 0.2$ and $x_{te} = 1.2$, was similar to that used in ref. [6]. The blockage was neglected, $h = 1$.

6 Turbine stage design

This is just an example that proves the capabilities of the implicit approach in dealing with high loaded and cambered blade geometries. The flowpath of the turbine stage and the tangential blade force distribution over the stator and rotor regions are shown in fig. 5. The function $F_b(\eta)$ for the rotor, with $\eta_{hub} = 0$ and $\eta_{tip} = 1$, is meant to produce radially constant specific work, provided that the unit mass flowrate does not approximately vary across the average rotor section [5]. Therefore, we prescribed $\rho u(\eta) = const = 0.220$ along the outlet section. Along the inlet section, we prescribed $T^0 = const = 1$, $p^0 = const = 1$, $\alpha = const = 0^o$ (meridional inlet flow) and $\beta(\eta) = \eta\beta_{tip} + (1-\eta)\beta_{hub}$. The rotational speed is 0.014. For sake of simplicity, we fastened both the rotor and stator streamsurfaces to meridional leading edges with no lean. The blockage and profile loss effects were neglected.

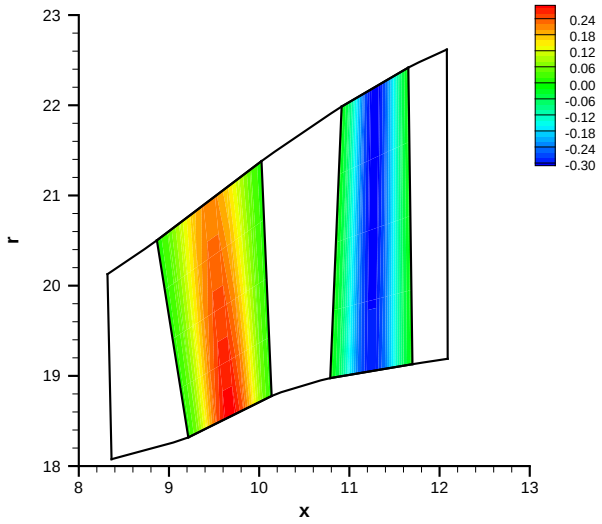

Fig. 5 Tangential blade force distribution

Fig. 6 shows the predicted three-dimensional geometry of the stator (red) and rotor (green) cambersurfaces. Fig. 7 displays the spanwise distribution of the relative blade-to-blade flow angle for the inlet and outlet sections of each blade row.

Finally figure 8 maps the predicted static pressure over the full flowpath. The radial variation of this quantity along the outlet section is negative because of the prescribed mass flowrate distribution. The enforcement of the mass flowrate, in fact, does not allow us to update the outlet pressure from the simple radial equilibrium eq., consistently with the constant work assumption. To avoid this drawback, we should prescribe a more realistic distribution of the mass flowrate along the outlet radius, with $\partial \rho u / \partial \eta < 0$. However, as previously stated, the present test case is only meant to provide a simple demonstration.

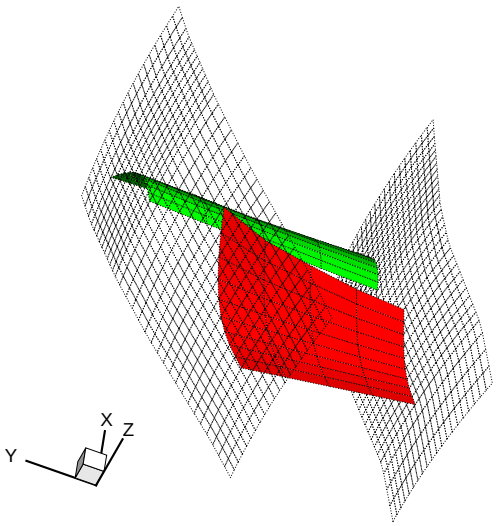

Fig. 6 Blade cambersurface geometry

The flow deflections proved in figs. 6 and 7 give an idea of the maximum camber levels currently achieved by the two-dimensional implicit scheme, 60^o to 90^o. For higher deflections, this meets numerical instabilities most likely due to the non-upwind treatment of the endwalls by eq. (8). On a two-dimensional cartesian grid, the scheme carries the limit loading levels only when spanwise periodical boundary conditions are prescribed, that is, when we suppress the wall effects and the cascades regain an infinite span. However, as pointed out in sec. 4, the ambiguity in the wall treatment does not relate to the adopted time marching procedure, but rather to the space discretization of the flowpath. Finally, we solved the linear systems that arise from the discretization of eqs. (2) and (8) by exact gaussian methods. This was done in order to use sufficiently high CFL values and avoid the further transient instability detected from the one-dimensional tests. To reach convergence on a 32x5 meridional grid, a P2 processor working at 350 MHz needed about 7 minutes CPU time.

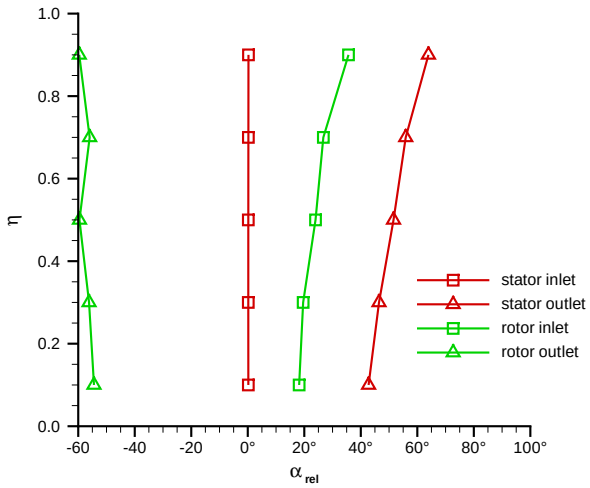

Fig. 7 Relative blade-to-blade flow angle

7 Concluding remarks

Thanks to the implicit upwind discretization of the Euler eqs. and streamsurface-flow slip eq., our numerical procedure succeeds in efficiently re-obtaining any theoretical inverse solution of the ideal cascade problem. This is possible even when the limit blade loadings are prescribed, which involve a sonic outlet flow at the maximum angle consistent with the enforced mass flowrate. However, even for moderately loaded and cambered turbine cascades, that could be provided by the explicit time marching procedure through non-reflective outlet conditions, the implicit procedure gains one order in convergence time and levels. Unfortunately, when we move to the complete throughflow formulation of the inverse problem, at very high flow deflections, the scheme does not keep the same numerical properties. We relate the matter to the adopted space

discretization, rather than the time marching procedure. On a finite volume grid, the scheme cannot identify the endwalls as characteristic lines for the surface-flow slip eq. The numerical instabilities that still arise above 90° flow deflections must be mainly due to such loss of upwind spirit along the endwalls. The discretization of the Euler eqs. through a finite difference implicit scheme will be dealt with by a subsequent paper.

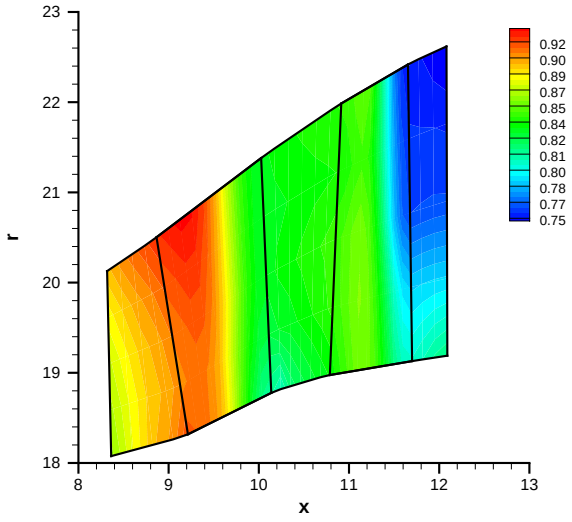

Fig. 8 Satic pressure map

Acknowledgements

This work has been partly funded by Regione Piemonte Italy (Bando regionale 2004-E57 and Bando regionale 2006-Corale) and partly by Avio Group Italy.

References

[1] Yao Z and Hirsch Ch. Throughflow model using 3D Euler or Navier-Stokes solvers. In *Turbomachinery - Fluid Dynamic and Thermodynamic Aspects*, VDI Berichte 1185, pp 51–61, 1995.

[2] Damle SV, Dang TQ and Reddy DL. Throughflow method applicable for all flow regimes. *Transactions of the ASME Journal of Turbomachinery*, Vol. 119, pp 256–262, 1997.

[3] Sturmayr A and Hirsch Ch. Throughflow model for design and analysis integrated in a three-dimensional Navier-Stokes solver. *Proceedings of the IMechE Part A Journal of Power and Energy*, Vol. 213, No. 4, pp 263–273, 1999.

[4] Simon J and Léonard O. A throughflow analysis tool based on the Navier-Stokes equations. In *ETC 6th European Conference on Turbomachinery*, Lille (F), 2005.

[5] Bena C, Larocca F and Zannetti L. Design of multi-stage axial flow turbines and compressors. *Proceedings of the IMechE 1999 3rd European Conference on Turbomachinery*, London (UK), paper C557/047/99, pp 635–644, 1999.

[6] Zannetti L and Pandolfi M. Inverse design technique for cascades. NASA Contractor Report 3836, 1984.

[7] Rosa Taddei S, Larocca F and Bertini F. Inverse design of high lift cascades by implicit upwind schemes. In *XVIII Congresso AIMETA di Meccanica Teorica e Applicata*, Brescia (I), paper FL06-1, 2007.

[8] Ferlauto M, Iollo A and Zannetti L. Set of boundary conditions for aerodynamic design. *AIAA Journal*, Vol. 42, No. 8, pp 1582–1592, 2004.

[9] Zannetti L and Larocca F. Inverse methods for 3D internal flows. AGARD Report 780, 1990.

[10] Rudy DH and Strickwerda JC. A non reflecting outflow boundary condition for subsonic Navier-Stokes calculations. *Journal of Computational Physics*, Vol. 36, pp 55–70, 1980.

[11] Wu CH. A general through flow theory of fluid flow with subsonic or supersonic velocities in turbomachines of arbitrary hub and casing shapes. NACA Technical Note 2302, 1951.

[12] Rosa Taddei S and Larocca F. Axisymmetric design of axial turbomachinery: an inverse method introducing profile losses. *Proceedings of the ETC 7th European Conference on Turbomachinery*, Athens (GR), paper 82, pp 645–655, 2007.

[13] Rai MM and Chackravarthy SR. An implicit form for the Osher upwind scheme. *AIAA Journal*, Vol. 24, No. 5, pp 735–743, 1986.

[14] Pulliam TH. Efficient solution methods for the Navier-Stokes equations. Lecture series in Numerical Techniques For Viscous Flow Computa-

tion In Turbomachinery Bladings, Von Karman Institute for Fluid Dynamics, Bruxelles (BE), 1986.

[15] Chackravarthy SR and Osher S. Numerical experiments with the Osher upwind scheme for the Euler equations. *AIAA Journal*, Vol. 21, No. 9, pp 1241–1248, 1983.

[16] Pandolfi M. A contribution to the numerical prediction of unsteady flows. *AIAA Journal*, Vol. 22, No. 5, pp 602–610, 1984.

[17] Deconinck H. A survey of upwind principles for the multidimensional Euler equations. Lecture series in Computational Fluid Dynamics, 1987-04, Von Karman Institute for Fluid Dynamics, Bruxelles (BE), 1987.

[18] Di Mascio A. *Simulazione di flussi vorticosi mediante il modello di flusso comprimibile non viscoso*. Tesi di Dottorato di Ricerca in Meccanica applicata, Università di Roma (I), 1992.

Appendix: list of symbols

x, r	axial, radial coordinate
ϑ, z	tangential coordinate
ξ, η	geometrical coordinates
$\vec{i}$, $\vec{j}$, $\vec{k}$	axial, radial, tangential unit vector
t	time
$\vec{V}$	speed vector
u, v, w	axial, radial, tangential speed
$\tilde{u}$, $\tilde{v}$	covariant speed components
α, β	blade-to-blade, ramp flow angle
λ	wave speed
Ma, a	Mach number, sound speed
ρ, p, T	density, pressure, temperature
E, H, S	internal energy, enthalpy, entropy
$\vec{f}_b$, $\vec{f}_v$	blade force, viscous force vector
F_b	blade loading
ω	rotational speed
h	tangential unit free passage
c, δ	blade chord, blade thickness
n, σ	blade number, cascade solidity
$\Delta\sigma$, $\Delta\ell$	cell area, cell side

Subscripts and superscripts

x, r	axial, radial component
ϑ, z	tangential component
exh	exhaust
inl, out	inlet, outlet section
le, te	leading edge, trailing edge section
hub, tip	hub, tip
rel	relative quantities
0	total quantities

Copyright Statement